Laser-Driven Neutron Generation with Near-Critical Targets and Application to Materials Characterization

F. Mirani, A. Maffini,[*] and M. Passoni

Politecnico di Milano, Via Ponzio 34/3, Milan I-20133, Italy

Laser-driven neutrons arouse outstanding interest because of their promising uses in several fields, from basic science to materials inspection. Many experiments achieved neutron yields [$10^8 - 10^{10}$ n/(sr s)] suitable for applications. These results were obtained by exploiting high-energy (approximately 10–100 J) lasers working at low repetition rates. Instead, adopting advanced target configurations like near-critical double-layer targets (DLTs) and compact, commercial lasers was slightly considered. Here, a theoretical study is performed to address neutron generation with commercial (40–400 TW, 1–15 J) systems and DLTs. We investigate proton acceleration and interaction with various materials to induce (p, n) reactions. DLTs allow achieving 1–2 orders of magnitude larger neutron yields and maximum energies 3 times higher than with single-layer targets. Then, the feasibility of two materials characterization techniques, namely fast neutron activation analysis and pulsed fast neutron resonance radiography, is assessed. The results indicate that they can be performed with commercial lasers and DLTs.

I. INTRODUCTION

Laser-driven radiation sources represent a well-established research topic [1,2]. They exploit the interaction between ultrashort, superintense ($I > 10^{18}$ W/cm^2) laser pulses and targets of various natures to accelerate electrons and ions. The adopted laser technology [3] includes both 10s fs time duration, 1–15 J energetic pulses provided at a high repetition rate (up to 10 Hz) and longer (approximately ps) more energetic (i.e., 10–100 J) systems working at a lower repetition rate (≤ 0.1 Hz). Besides, different materials like gaseous, liquid and solid targets have been studied [4]. Among the various configurations, micrometric thick solid foils allow accelerating electrons and ions at energies ranging from a few up to tens of MeV, according to the laser power. Particles, emitted via the target normal sheath acceleration (TNSA) mechanism, are characterized by an ultrafast dynamic, broad energy spectrum and angular distribution. Notably, using advanced double-layer targets (DLTs) represents a viable route to increase their number and energy [5–9]. Indeed, a low-density layer in front of the solid foil enhances the laser absorption, leading to a more efficient TNSA [10]. Moreover, the interaction between the accelerated electrons and ions and proper converter materials can be exploited to generate energetic γ rays [11,12], positrons [13], and neutrons [14,15] as well. The use of these particles for laser-driven materials characterization

techniques like particle-induced x-ray emission (PIXE) [16–19], energy dispersive x-ray spectroscopy (EDX) [18,20], x-ray fluorescence spectroscopy [19,21], positron annihilation lifetime spectroscopy [22], photon activation analysis [23] and radiography [24] are attracting increasing interest.

Focusing on neutron production, several approaches based on the so-called *pitcher-catcher* configuration can be adopted. For instance, bremsstrahlung photons, emitted from the interaction between high-energy electrons and a high-Z converter medium, can further interact with the nuclei of the material by inducing photonuclear reactions and consequent neutron generation [25,26]. Another strategy consists of the use of deuterated targets to achieve $d(d,n)^3$He, ^{7}Li$(d,n)^8$Be, and ^{9}Be$(d,n)^{10}$B reactions [27–29]. Lastly, neutrons are generated via proton acceleration and ^{9}Be$(p,n)^9$B, ^{7}Li$(p,n)^7$Be, and ^{63}Cu$(p,n)^{63}$Zn nuclear reactions [29–32]. As shown in Ref. [26], exploiting 1–15 J energetic pulses, approximately 10^4–10^6 n/(sr shot) is achievable. On the other hand, with 100s J laser energy, approximately 10^8–10^{10} n/(sr shot) are generated. Laser-driven neutron sources are worthy of consideration for several applications like inspection of nuclear materials [33], probing of extreme states of matter [34], neutron resonance transmission spectroscopy [35], fast neutron activation analysis (FNAA) [36] and pulsed fast neutron resonance radiography (FNRR) [37,38]. We point out that most applications require high-energy lasers to achieve the necessary neutron fluxes exploiting single-layer targets.

*alessandro.maffini@polimi.it

Within the materials elemental characterization and security frameworks, two interesting techniques relying on fast neutrons are FNAA and pulsed FNRR. FNAA [39–41] usually exploits fast neutrons from fusion reactions, mainly at 14-MeV energy. They are obtained with relatively compact *D-T* generators providing 10^7–10^8 n/s. Neutrons irradiate samples having unknown elemental composition inducing nuclear reactions and the subsequent emission of characteristic γ rays. While FNAA is used to identify many elements, its most important application is the determination of oxygen and nitrogen content in various matrices [42]. Another appealing technique for H, N, C, and O identification is pulsed FNRR [43,44]. Neutrons with a broad energy spectrum (i.e., from 0.5 to 10 MeV) irradiate a sample placed at some meters distance from the pulsed source. The energy and position of the transmitted neutrons are detected by exploiting position-sensitive time-of-flight (TOF) systems. Compact and reliable versions of these detectors are the object of research. Pulsed FNRR allows the spatial distribution reconstruction of the elements on the projection plane. It requires a minimum neutron flux of approximately 10^4 n/(cm^2 s) at an approximately 3-m distance from the source [45] [i.e., approximately 10^9 n/(sr s)]. Therefore, it is under development considering particle accelerators and high-energy (i.e., approximately 100 J) laser-driven neutron sources. A pathway to significantly decrease the laser requirements for pulsed FNRR is to exploit advanced DLTs. Recently, the use of these targets for neutron generation was numerically investigated considering $I = 2 \times 10^{21}$ W/cm^2 (normalized intensity $a_0 \approx 30$) [46]. However, considering less energetic pulses from commercial fs lasers could be of exceptional significance, in terms of costs and size, for illegal material detection (e.g., explosives and drugs) via pulsed FNRR in customs, airports, and borders. Moreover, high-energy ns lasers are characterized by intense electromagnetic pulses (EMPs). EMPs can be a challenging aspect for neutron detectors exploited in laser-driven FNRR [37]. The same key challenge should be mitigated by exploiting 1–15 J energy lasers.

The generation of neutrons exploiting compact (i.e., 5–15 m^2), fs time duration laser systems commercially available is investigated in this work. Then, we examine the applicability of the laser-driven neutron sources to FNAA and pulsed FNRR. Lastly, a case study of pulsed FNRR is fully simulated via Geant4 Monte Carlo (MC) simulations. To these aims, DLTs and different converter materials (i.e., Be, LiF, and Cu) are considered for the proton acceleration and generation of high-energy neutrons, respectively. The laser-driven proton source is described by exploiting a recently developed theoretical model [47]. The interaction between the protons and converter materials is studied via MC simulations [48,49] and theoretical calculations. Notably, simple scaling laws are obtained via analytical approximations. Finally, we show

that commercially available 1–15 J energy laser systems coupled with DLTs and converter materials are suitable for neutron-based materials inspection and analysis.

II. RESULTS AND DISCUSSION

The first goal of this study is to investigate laser-driven neutron generation considering conventional single-layer targets and DLTs, a pitcher-catcher configuration and a suitable range of laser intensities. To suitably describe the generated neutron properties, we evaluate different quantities. They are the neutron energy-angle distribution $Y(E_n, \Omega)$ and the neutron spectrum $Y(E_n)$ per unit incident proton, the total neutron yield Y_T and the neutron current $\dot{N}_n$. The analysis will be carried out through theoretical models, Monte Carlo simulations and scaling obtained from experimental data reported in the literature.

From a theoretical standpoint, the energy-angle distribution can be expressed with the relation:

$$Y(E_n, \Omega) = \frac{1}{N_p} \frac{dN_n}{dE_n \, d\Omega} = \frac{N_{Av}}{M} \rho$$
$$\times \int_0^\infty f(E_p) \int_0^{E_p} \frac{\sigma(E, E_n, \Omega)}{S_p(E)} \, dE \, dE_p, \quad (1)$$

where E_n is the neutron energy, Ω is the solid angle, N_{Av} is Avogadro's number, M is the atomic mass, ρ is the density, $f(E_P)$ is the proton spectrum normalized to the total number of protons N_p, $S_p(E)$ is the proton linear stopping power of the converter material and $\sigma(E, E_n, \Omega)$ is the double-differential cross section for neutron generation. The neutron spectrum per unit incident proton $Y(E_n) = dN_n/(dE_n N_p)$ is provided by the same analytical expression of Eq. (1), but considering the differential cross section $\sigma(E, E_n)$. Analogously, the total neutron yields can be evaluated with the integral cross section $\sigma(E)$:

$$Y_T = \frac{N_n}{N_p} = \frac{N_{Av}}{M} \rho \int_0^\infty f(E_p) \int_0^{E_p} \frac{\sigma(E)}{S_p(E)} \, dE \, dE_p \quad (2)$$

and the generated neutron current is provided by

$$\dot{N}_n = RR \, N_p \, Y_T \quad (3)$$

being *RR* the laser repetition rate.

A. Experimental and modeling of proton acceleration with DLTs

To evaluate the quantities defined by Eqs. (1)–(3), we need to express the laser-driven proton spectrum $f(E_p)$ as a function of the laser and target properties. In TNSA, proton spectra are monotonically decreasing with E_p, and present a well-defined maximum (or *cut-off*) energy $E_{p,\max}$. The first part of Table I summarizes the main

TABLE I. Summary of experimental data from the literature and model results for the laser-driven proton sources exploited in this work. Cir, lin, CF, CN, and CH stand for circular, linear, carbon foam, carbon nanotubes, and carbon homogeneous, respectively.

	Laser parameters					DLT parameters			$E_{p,\max}$ (MeV)	
	a_0	E_L (J)	Contrast	Incidence (deg)	Polarization	r_{nc} (μm)	ρ (n_{cr})	Structure	DLT	Bare target
[8]	0.3	2	10^{-8}	10	⋯	12	1.0	CF	1.3	0.3
[8]	0.64	2	10^{-8}	10	⋯	12	1.0	CF	1.6	1.2
[8]	0.77	2	10^{-8}	10	⋯	12	1.0	CF	1.9	1.8
[8]	0.21	2	10^{-12}	10	⋯	12	1.0	CF	1.4	0.6
[8]	0.43	2	10^{-12}	10	⋯	12	1.0	CF	2.2	1.4
[57]	9.7	4 - 5	10^{-9}	0	cir	5.0	2.0	CN	15.0	10
[57]	9.7	4 - 5	10^{-9}	0	lin	5.0	2.0	CN	29.0	12
[7]	9.7	4–5	10^{-11}	0	lin	8.0	0.5	CN	30.0	12.0
[5]	12.8	1–7.4	10^{-11}	30	lin	8.0	1.2	CF	30.0	18.0
[5]	13.1	1–7.4	10^{-11}	30	cir	8.0	1.2	CF	30.0	10.0
[5]	13.8	1–7.4	10^{-11}	30	lin	8.0	1.2	CF	30.0	22.0
[9]	15.3	1.9	10^{-10}	0	lin	4.0	3.2	CF	18.5	9.5
[9]	15.3	2.0	10^{-10}	45	lin	4.0	3.2	CF	13.4	10.3
[58]	16.0	9.2	10^{-11}	2.4	lin	40.0	0.4	CN	60.0	22.0
Model	5	0.6	⋯	0	lin	8.0	1.0	CH	8.64	1.96
Model	10	2.3	⋯	0	lin	11.0	1.0	CH	24.3	5.69
Model	15	5.0	⋯	0	lin	13.2	1.0	CH	40.6	9.95
Model	20	9.0	⋯	0	lin	15.1	1.0	CH	59.2	14.6
Model	25	14.0	⋯	0	lin	16.8	1.0	CH	71.36	19.5

experimental results from the literature comparing the performances of bare targets and DLTs. Near-critical layers having the required densities and thicknesses can be obtained through the deposition of carbon foams (CFs) [50–52] or carbon nanotubes (CNs) [53] on bare substrates. Depending on the laser and target parameters, the maximum energy increment achieved with DLTs can span from approximately 1 to 3–4, relative to the proximity to the optimal configuration.

To link $E_{p,\max}$ and the spectral shape to laser and DLT properties, we exploit the theoretical model developed by Pazzaglia *et al.* [47]. It allows describing the laser propagation through self-focusing in a homogeneous near-critical density layer and reflection at the substrate interface. The model is valid for $a_0 < 50$, pulse duration $\tau \sim 10$s fs, near-critical layer density $n_{nc} < 20$, and normal incidence. These constrains allow neglecting the direct laser absorption by plasma ions, ensuring relativistic ponderomotive self-focusing and preserving self-focusing axial symmetry. Under these conditions, the model validity was tested via comparison with experimental data and PIC simulations presented in Ref. [47]. Starting from the parameters of the laser (i.e., wavelength λ, a_0, spot waist FWHM w, τ and polarization) and target (i.e., n_{nc} and substrate thickness r_{sub}), we perform an optimization over the near-critical layer thickness r_{nc} to maximize $E_{p,\max}$.

The results from the model are listed in the second part of Table I. We assume linearly polarized laser pulses having $\lambda = 0.8$ μm, $a_0 = 5, 10, 15, 20, 25$, $w = 4.7$ μm, $\tau = 30$ fs and normal incidence according with the model

requirements. The laser energies are compatible with the parameters of existing commercial high-intensity lasers [54,55] working at a 1–10-Hz repetition rate. The DLTs have $n_{nc} = 1$ in units of critical density and 1-μm substrate thickness. Maximum energies with single-layer targets agree with the scaling laws presented in the literature [56]. Overall, the enhancement of $E_{p,\max}$ achieved with the DLT configuration via model optimization is coherent with best experimental results reported in Table I. The model also provides the mean energy of the hot-electron population T_e. It lies between 0.4–3.0 MeV and 1.6–11.0 MeV for bare targets and DLTs, respectively.

Different approaches are possible for what concerns the analytical expression of proton spectra. One possibility is to describe the spectra as an exponential with a cutoff at $E_{p,\max}$ and an effective temperature T_p:

$$f(E_p) = \frac{dN_p}{dE_p} \propto \exp{-\frac{E_p}{T_p}}. \tag{4}$$

Despite its simplicity and handiness, this choice will introduce T_p as a free parameter, which cannot be easily related to laser and target conditions. As an alternative, one can exploit the relation proposed by Mora in Ref. [59]:

$$f(E_p) = \frac{dN_p}{dE_p} \propto \frac{1}{\sqrt{E_p \, T_{\text{eff}}}} e^{-\sqrt{2E_p/T_e}} \tag{5}$$

for $E_p \leq E_{p,\max}$. Here T_{eff} is the electron temperature, a quantity that can be estimated as the average electron

energy T_e even far from thermodynamic equilibrium [60]. In this way, one can get the proton energy distribution as a function of laser intensity and target configuration, as shown in Fig. 1(a) for $a_0 = 5, 10, 15, 20,$ and 25.

The proton angular divergence cannot be estimated with the model. Experimental data show angular distributions peaked in the forward direction and subject to a certain degree of uncertainty. Exploiting bare targets, the average angular aperture is set around $\pm 10°$–$20°$ [61,70,71,75,77]. Analogous values have been observed with DLTs [9].

Accordingly, we reasonably assume an average angular divergence of $\pm 20°$. It is worth mentioning that this value mildly affects our study on neutron generation since the converters are large enough (see the next section) so that all primary protons interact with the material.

Before proceeding, two nonidealities that are not directly taken into account by the model are worthwhile to mention. Firstly, the presence of a prepulse can alter the ideal TNSA mechanism both with single-layer targets and DLTs. Exploiting submicrometric thick bare targets and
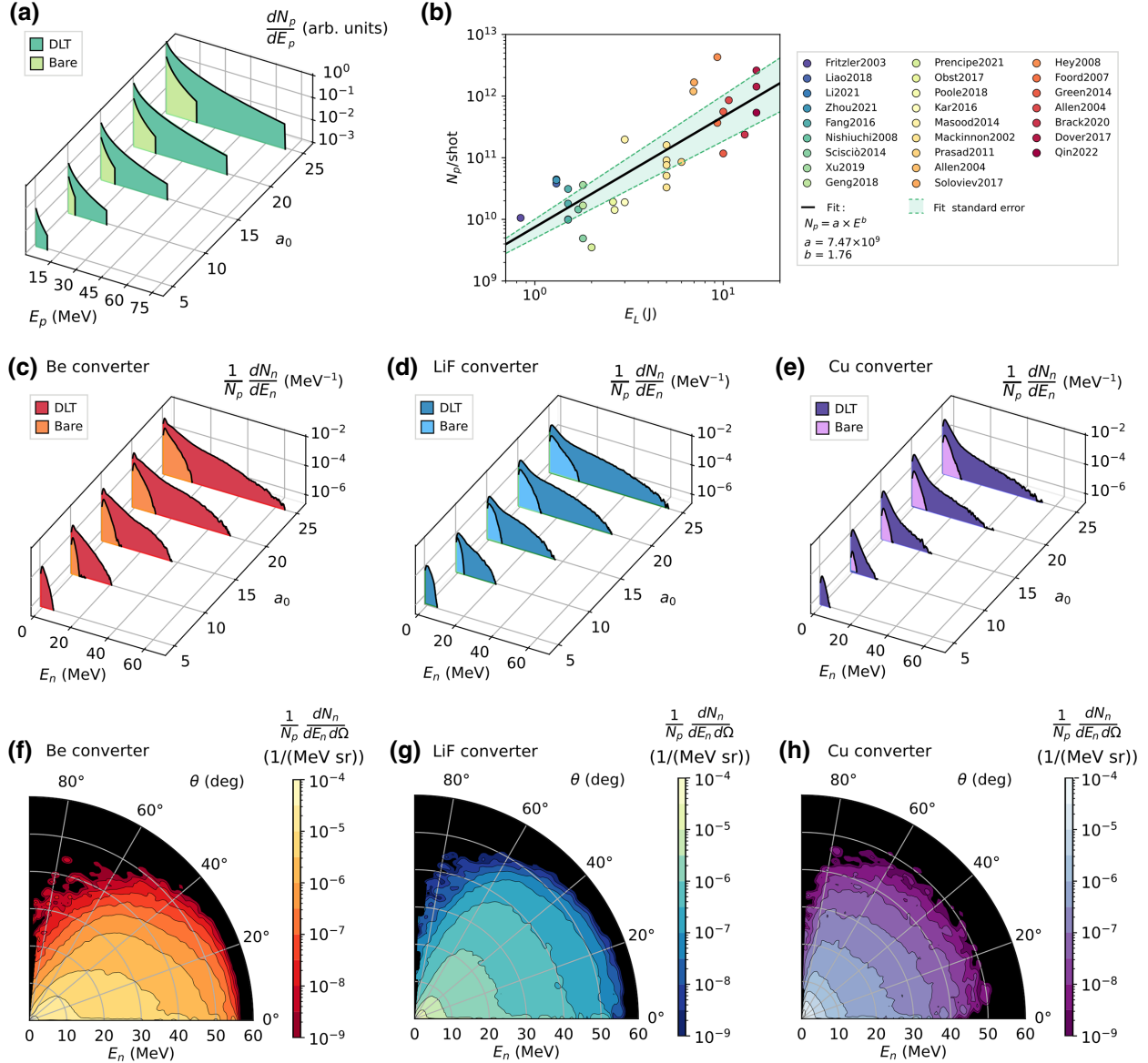

FIG. 1. Monte Carlo simulation of laser-driven neutron generation. (a) Proton energy spectra for $a_0 = 5, 10, 15, 20, 25$, single-layer targets and DLTs. (b) Number of accelerated protons per unit shot as a function of laser energy E_L obtained from the literature [9,61–84]. The black line is the exponential fit, and the filled green region represents the fit standard error (i.e., $\pm$ standard deviation of the fitting parameters a and b). (c)–(e) Energy spectra of the generated neutrons retrieved with the MC for Be, LiF, and Cu converters exploiting the single-layer and DLT proton energy spectra. (f)–(h) Energy-angle distributions of the neutrons emitted from the rear surface of the converters for the case $a_0 = 20$ and DLT.

laser contrast approximately 10^{-6}, the prepulse can damage the solid before the main peak arrival [85]. On the other hand, for approximately 10^{-10} temporal contrast, the TNSA mechanism develops without nonidealities. Also in the case of DLTs, low contrast conditions have a detrimental effect in terms of proton energy enhancement [8]. Thus, to preserve the model validity, proper contrast conditions (i.e., below approximately 10^{-9}) must be assumed. Secondly, the presence of a nanostructure having inhomogeneity scale greater than the laser wavelength can perturb the electromagnetic field distribution. When required, this effect can be included in the model via the introduction of a correction factor as discussed in Ref. [47]. Here, sufficiently uniform near-critical layers (e.g., carbon nanotube foams [7,57]) to neglect this correction are considered. We do not elaborate further these aspects since it is beyond the aim of our work.

A reasonable assumption about the number of accelerated protons is required to evaluate the performance of the laser-driven neutron source and assess the FNAA and FNRR feasibility. Indeed, accordingly to Eq. (3), the secondary neutron current is directly proportional to the number of primary protons per shot. Reliable values cannot be achieved from the model, nor from PIC simulations. Indeed, they are dependent on the distribution and composition of the hydrogenated contaminant layer on the backside of the target. Therefore, we perform a scaling for N_p/shot as a function of the laser energy E_L considering experimental proton spectra available in the literature. In line with the sources under consideration, we include only experimental works with laser energies lower than 15 J and $\tau < 100$ fs. Due to the more significant data availability in the literature, we account only for experiments performed with single-layer targets rather than DLTs. The experimental data are obtained with detectors (e.g., radiochromic films [68]) that provide the total number of protons per unit of energy regardless of the transverse beam profile. We discard data retrieve with Thompson parabolas and TOF spectrometers since they give information along a well-defined direction and a narrow solid angle. The experimental data are interpolated with Eq. (5), assuming proton energies ranging from the minimum required for neutron generation (i.e., 2 MeV) to the cutoff values. Then, we evaluate the total proton number by integrating the fitted spectra. The results are summarized in Fig. 1(b). A clear growing trend in the number of accelerated protons per shot as a function of the laser energy can be appreciated. The spread of the data is related to different aspects that are not considered in this analysis. Actually, we do not discern between laser polarization, focal spot size, target material, and thickness. Moreover, since protons are accelerated from the contaminant layer on the rear side of the target, their number is intrinsically subject to a certain degree of uncertainty. Nevertheless, the estimation of the proton number per shot is satisfactory for the aims of this work.

The black curve reported in Fig. 1(b) is an exponential fit:

$$N_p/\text{shot} = a\, E_L^b, \qquad (6)$$

where $a = (7.47 \pm 2.57) \times 10^9$ and $b = 1.76 \pm 0.22$. We use Eq. (6) for the accelerated number of protons per shot and the spectra of Fig. 1(a) to explore neutron generation (via MC simulations) in the following. With a view to assess the laser-driven FNAA and FNRR feasibility exploiting bare targets, Eq. (6) is accurate. Moreover, considering DLTs, the scaling provides a safe estimation. Indeed, besides higher energies, DLTs also allow the proton number to be enhanced by several times [5,9].

B. Modeling of the laser-driven neutron sources

We proceed by investigating laser-driven neutron generation, considering Be, LiF, and Cu converters, exploiting Geant4 MC simulations. A detailed description of the MC implementation is provided in Appendix A. Ten simulations [one for each proton energy spectrum reported in Fig. 1(a)] have been performed. The energies of the primary particles are extracted from the corresponding proton spectra. The proton angular divergence to the converter normal direction is sampled from a uniform distribution between $\pm 20°$. The converter thicknesses are equal to the ranges of the cutoff energy protons. For instance, considering the case study $a_0 = 25$ and DLT, the converter thicknesses are 2.8, 2.0, and 0.7 cm for Be, LiF, and Cu, respectively. It is a reasonable choice to achieve the highest neutron yields since 1–100 MeV energy neutrons are slightly self-attenuated in cm-thick materials. The distance between the source and the converter front side and the lateral size is 4 cm.

The energy spectra $Y(E_n)$ of the generated neutrons are reported in Figs. 1(c)–1(e) for the Be, LiF, and Cu converters, respectively. Considering Be and LiF materials, the spectra have a quasiexponential shape, and the maximum energies correspond to the cutoff values of the incident protons. As a result, the maximum neutron energies for the DLTs are almost 3.5 times higher than those obtained with single-layer targets. On the other hand, the maximum neutron energy achieved with the Cu converter is slightly lower than those obtained with Be and LiF. We also characterize the energy-angle distribution of neutrons emitted in the forward direction $Y(E_n, \Omega)$. They are reported in Figs. 1(f)–1(h) for the $a_0 = 20$ and DLT case studies. $Y(E_n, \Omega)$ is not uniform for neutrons emitted from the Be converter. Indeed, it is rather piked along the converter normal direction. In the case of LiF and Cu converters, the distributions are practically uniform for divergence angles lower than $60°$. Arguably, applications requiring intense neutron fluxes along the beam axis (e.g., pulsed FNRR) could benefit from the adoption of Be converters. On the other hand, LiF and Cu converters should be favored when

uniform irradiation on large surfaces is demanded (e.g., FNAA).

While evaluating neutron energy-angle distributions and energy spectra requires MC simulations, we aim at finding an explicit, analytical expression for the total yield Y_T. Indeed, it can help make quick estimates as a function of experimental parameters and to guide the design of future experiments. This will be the aim of the final part of this section. Firstly, one can look for some suitable approximation of the integrals in Eq. (2). Let us define the differential yield $g(E)$ and the monoenergetic yield $h(E)$ as

$$g(E) = N_{at} \frac{\sigma(E)}{S(E)} \tag{7}$$

and

$$h(E_p) = \int_0^{E_p} g(E)\,dE = \int_0^{E_p} N_{at} \frac{\sigma(E)}{S(E)}\,dE. \tag{8}$$

In which $N_{at} = \rho\,N_{Av}/M$ in the atomic density of the converter. The stopping power $S(E)$ for laser-accelerated protons can be expressed through the nonrelativistic Bethe-Bloch formula:

$$S(E) \approx 2\pi\,R_e^2\,m_e c^2\,\frac{m_p c^2}{E}\,\ln\left(\frac{4E}{I}\frac{m_e}{m_p}\right)n_e, \tag{9}$$

where E is the proton energy, R_e is the classical electron radius, c is the speed of light in vacuum, m_e and m_p are the electron and proton rest mass, I is the mean excitation energy, and n_e is the electron density in the converter material.

To find an analytical expression for the integral $\int f(E_p)\,h(E_p)\,dE_p$, $f(E_p)$ being the distribution function of Eq. (5), the monoenergetic yield $h(E)$ should be expressed as a polynomial function of E_p. We propose a very simple polynomial approximation for the differential (and hence for monoenergetic) neutron yields

$$\begin{aligned} g(E) &= C\,(E - E_0)^p\,H(E - E_0) \\ h(E_p) &= \frac{C}{1+p}\,(E - E_0)^{(p+1)}\,H(E - E_0), \end{aligned} \tag{10}$$

where E_0 is a threshold energy, C a proportionality constant, and p an integer or semi-integer exponent. $H(x)$ represents the Heaviside step function and expresses the fact that the total cross section for neutron generation (reported in Appendix A) must be zero for energies below the threshold value. To express $g(E)$ and $h(E)$ in terms of physical constants (R_e, $m_e c^2$, $m_p c^2$), converter properties (n_e, I) and free model parameters (E_0, C_σ, ε, p) the logarithmic dependence of Bethe stopping power is approximated by the constant value $\ln\left(4\varepsilon/I m_e/m_p\right)$

TABLE II. Fitted free parameters for the converter materials.

Converter	C (MeV^{-p-1})	E_0 (MeV)	p
Be	$1.57 10^{-4}$	2	0.5
Cu	$1.12 10^{-5}$	5.25	1
LiF	$9.39 10^{-6}$	0	1

(ε being a constant with the dimension of an energy), so that one can combine Eqs. (9), (7), and (10), to get the following relation:

$$\begin{aligned} g(E) &\approx H(E - E_0)\,\frac{N_{at}}{2\pi\,R_e^2\,m_e c^2\,m_p c^2} \\ &\quad \times \frac{C_\sigma}{n_e\,\ln\left(\frac{4\varepsilon}{I}\frac{m_e}{m_p}\right)}\,(E - E_0)^p. \end{aligned} \tag{11}$$

The free parameters can be determined by fitting Eq. (11) to some reference values of Eq. (7): this can be done, for instance, by considering the experimental values of $\sigma(E)$ and $S(E)$ for each converter material. Results from the fitting procedure for Be, Cu, and LiF converters are given in Table II.

If the proton distribution is modeled with an exponential proton spectrum [Eq. (4)] the total neutron yield is readily obtained by putting Eq. (11) in Eq. (2):

$$\begin{aligned} Y_T &\approx C\,\frac{1}{1+p}\,\frac{\exp\left(\frac{-E_0 + E_{p,\max}}{T}\right)}{\exp\left(\frac{E_{p,\max}}{T}\right) - 1} \\ &\quad \times \left(\Gamma(p+2) - \Gamma_i\left(p+2, \frac{E_{p,\max} - E_0}{T}\right)\right)\,T^{p+1}, \end{aligned} \tag{12}$$

where Γ and Γ_i are the Euler's Γ function and the incomplete Γ function respectively, and the proportionality constant C is given by

$$C = \frac{N_{at}}{n_e}\,\frac{1}{2\pi\,R_e^2\,m_e c^2\,m_p c^2}\,\frac{C_\sigma}{\ln\left(\frac{4\varepsilon}{I}\frac{m_e}{m_p}\right)}. \tag{13}$$

The choice of a proton spectrum of the type described by Eq. (5) results, however, in a much more complicated expression. As an example, in the case of $p = 1$ (as for Cu and LiF converter, see Table II) one gets the following expression:

$$Y_T \approx C \, \frac{e^{-\frac{\sqrt{2}(\sqrt{E_0}+\sqrt{E_{p,\max}})}{\sqrt{T}}}}{2\sqrt{2}\left(1 - e^{-\sqrt{2}\sqrt{\frac{E_{p,\max}}{T}}}\right)}$$

$$\times \left(2\left(6\sqrt{E_0 T^3} + \sqrt{2}T(2E_0 + 3T)\right)e^{\sqrt{2}\sqrt{\frac{E_{p,\max}}{T}}}\right.$$

$$- e^{\sqrt{2}\sqrt{\frac{E_0}{T}}}\left(\sqrt{2}E_0^2 - 2\sqrt{2}E_0(E_{p,\max} + T)\right.$$

$$- 4E_0\sqrt{E_{p,\max}T} + \sqrt{2}\left(E_{p,\max}^2 + 6E_{p,\max}T + 6T^2\right)$$

$$\left.\left.+ 4\sqrt{E_{p,\max}T}\,(E_{p,\max} + 3T)\right)\right). \tag{14}$$

A useful simplification is achieved under the assumption of $E_{p,\max} \gg T$, E_0, resulting $Y_T \approx \int_{E_0}^{\infty} f(E_p)h(E_p)dE_p$ (that is to say, the contribution of protons with $E > E_{p,\max}$ to the total neutron yield is negligible). While $E_{p,\max} \gg T$ is an intrinsic feature of TNSA process, $E_{p,\max} \gg E_0$ is verified for converter materials in which the energy threshold for neutron production is relatively low, such as those considered in this work. In this limit, the total neutron yield is given by

$$Y_T \approx C \, \pi^{-1/2} \, \Gamma(p+1) \, 2^{\frac{1}{4}(2p+5)}$$

$$\times E_0^{\frac{1}{4}(2p+3)} \, T^{\frac{1}{4}(2p+1)} K_{(p+3/2)}\left(\sqrt{\frac{2E_0}{T}}\right), \tag{15}$$

where $K_\alpha(x)$ is the modified Bessel function of the second kind, of order α, of argument x. The final step is to express T as a function of the laser and target parameters following the model proposed in Ref. [47]. For the purpose of this work we assume that the electron temperature depends on the normalized vector potential $a0$ as in the modified ponderomotive scaling [86]:

$$T \approx m_e c^2 \, Q_t \, (\sqrt{1 + a_0^2} - 1), \tag{16}$$

where the target configuration affects the value of the proportionality constant Q_t. While this scaling is generally employed in the case of simple foil targets, its extension to more complex target configurations is challenging. Indeed, following the model proposed in Ref. [47], the mean electron energy in DLT configuration should result from the averaging of two different electronic populations in a nonstraightforward way. Nevertheless, even a crude extrapolation as Eq. (16) can provide a reasonably accurate estimation of T ($\pm 10\%$ of the value given by the model in Ref. [47]) over the whole range of laser intensity considered in this work ($5 \geq a_0 \leq 35$), provided that $Q_t = 0.24$ for bare targets and $Q_t = 0.83$ for DLTs.

To conclude, we study the asymptotic behavior of Y_T for $a_0 \gg 1$. In this limit $T \approx Q_t \, m_e c^2 \, a_0 \gg E_0$, and hence

Eq. (15) becomes $Y_T \approx C \, T^p \left(2^{-p}\Gamma(2p+2)T - 2^{-p}E_0\Gamma(2p+1)\right)$. By comparison, Eq. (12) (total yield with exponential proton spectra) would be equivalent to $Y_T \approx C \, \exp(-E_0/T) \, T^{p+1} \, \Gamma(p+1)$ under the same assumption. In both cases the leading term in T is $\propto T^{p+1}$, meaning that $Y_T \propto a_0^{p+1}$ for sufficiently large values of a_0. Putting all together, the total neutron yield under the discussed assumptions is approximated by

$$Y_T \approx \frac{N_{at}}{n_e} \, \frac{1}{2\pi \, R_e^2 \, m_e c^2 \, m_p c^2} \, \frac{C_\sigma}{\ln\left(\frac{4\varepsilon}{I}\frac{m_e}{m_p}\right)} \, \frac{(2p)!}{2^p}$$

$$\times (m_e c^2 \, Q_t \, a_0)^p \left[(2p+1)m_e c^2 \, Q_t \, a_0 - E_0\right]. \tag{17}$$

In Fig. 2, we show a comparison among the total neutron yield calculated with Eq. (17) (solid lines), the numerical integration of Eq. (2) (dashed lines) and Geant4 simulations (filled points) for Be (left, red), LiF (middle, blue), and Cu (right, violet) converters and for bare targets (top) and DLTs (bottom). We note that the analytical approximations are remarkably close to numerical integration and MC results for each target configuration and converter material combination. Notably, the neutron yields with DLTs are 1–2 orders of magnitude higher than those obtained with single-layer targets. For the latter, no neutrons are generated for the $a_0 = 5$ condition regardless of the converter material, agreeing with already published simulation results [10]. Overall the highest neutron yields are achieved by exploiting Be converters and DLTs for all a_0 values.

Once we have fully characterized neutrons generated by commercial lasers, bare targets and DLTs, the second part of the work will be devoted to evaluating the feasibility of two materials characterization and inspection techniques, i.e., laser-driven FNAA and pulsed FNRR.

C. Assessment of laser-driven FNAA feasibility

The goal of this section is to assess the potential of laser-driven FNAA carried out with DLTs. To this aim, the sample activation achieved with a state-of-the-art D-T neutron generator and the laser-driven sources (characterized in the previous section) should be compared. Therefore, we perform MC simulations of sample irradiation with 14-MeV monoenergetic and laser-driven neutrons. The sample is a mixture of O, Fe, Al, and K isotopes. Thus, the $^{16}\mathrm{O}(n,p)^{16}\mathrm{N}$, $^{54}\mathrm{Fe}(n,p)^{54}\mathrm{Mn}$, $^{27}\mathrm{Al}(n,p)^{27}\mathrm{Mg}$, and $^{41}\mathrm{K}(n,\alpha)^{38}\mathrm{Cl}$ nuclear reactions exploited for FNAA purposes are considered. In Fig. 3(a), we report the ratio between the number of nuclear reactions obtained with the D-T generator Y_{DT} and laser-driven sources Y_{LD}. The results are provided for each converter material and value of a_0. Then, we take the average of the ratio Y_{DT}/Y_{LD} performed over the nuclear reactions for each value of a_0 and converter material.
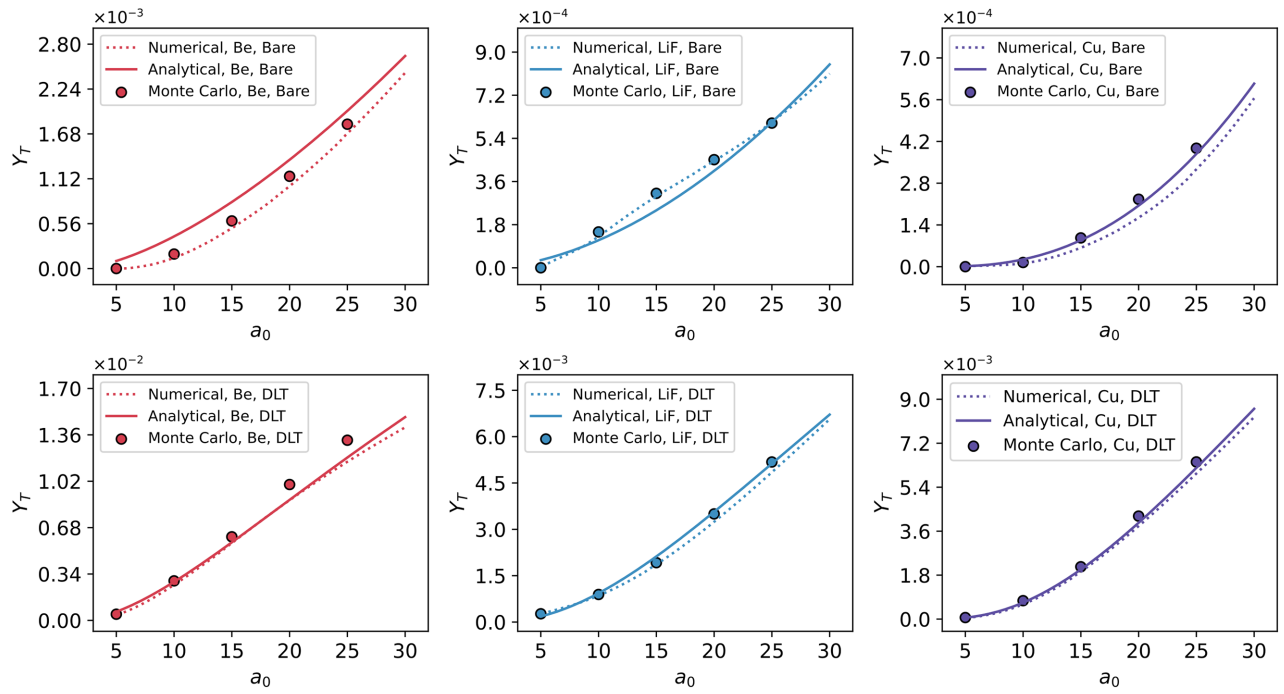
FIG. 2. Total neutron yields evaluated for bear targets (upper panels) and DLTs (lower panels). Data marked as points are obtained from MC simulations, dashed lines are retrieved from numerical integrals, and the continuous lines are the analytical expression of the yields.

To proceed, we assume a *D*-*T* neutron source providing $\dot{N}_{n,DT} = 5 \times 10^7$ n/s on the sample, and we consider the laser-driven neutrons emitted in the forward direction N_n/N_p [see Fig. 3(b)]. The average laser-driven proton current $\dot{N}_{p,\mathrm{req}}$ required to achieve the same sample activation induced with the *D*-*T* source is given by

$$\dot{N}_{p,\mathrm{req}} = \frac{\dot{N}_{n,DT}}{Y_{DT}/Y_{LD}\ N_n/N_p}. \tag{18}$$

The result is presented in Fig. 3(c) for each value of a_0 and converter material. As expected, the required laser-driven proton current is higher for lower laser intensity because the neutron yield is less. Then, by dividing the required proton current by the number of protons per laser shot from scaling Eq. (6), we can estimate the laser repetition rate needed to equal the activation with the *D*-*T* generator. The results are shown in Fig. 3(d) for a_0 starting from 10. We excluded the $a_0 = 5$ case study since the resulting repetition rates for any converter material were too high to be achieved with existing laser systems. For each value of a_0, we also report the nominal repetition rate (10, 5, and 1 Hz) of the corresponding commercial lasers [54,55].

Exploiting Be and LiF converters, the required repetition rates are lower than those achievable. Thus, considering commercial systems having $a_0 = 10 - 25$ and Be (or LiF) converters, laser-driven FNAA can be performed with comparable performances to conventional FNAA. In the case of $a_0 = 10$ and Cu converter, the required repetition

rate is one order of magnitude higher than that currently achievable. It is worth noting that the obtained results are conservative since we are considering the number of accelerated protons (and therefore neutrons) provided with single-layer targets.

D. Assessment of laser-driven FNRR feasibility

Pulsed FNRR exploits the characteristic features of the total neutron cross sections of H, C, N, and O in the 1–10 MeV energy range [see Fig. 4(a)]. Basically, the energy and position detection of the transmitted neutrons through a sample allows for mapping the low-*Z* elements. Pulsed FNRR is a more challenging technique to carry out than FNAA. Indeed, the source must satisfy several requirements (e.g., small spot size, short temporal duration, broad energy spectrum, and shot-to-shot stability) to guarantee a reliable measurement in a reasonable amount of time. Meeting these requirements using commercial sources, besides the availability of suitable neutron detectors, is the main obstacle to overcome. In this section, we verify some of the requirements for the considered laser sources. On the other hand, the development of suitable detectors for laser-driven FNRR (see Ref. [37,38]) is beyond the scope of this work and will be addressed in future studies.

A source prerequisite performing pulsed FNRR concerns its time duration. For a source-detector distance of approximately 3 m, it must be of the order of a few ns (or shorter) to ensure a sufficiently high resolution to resolve
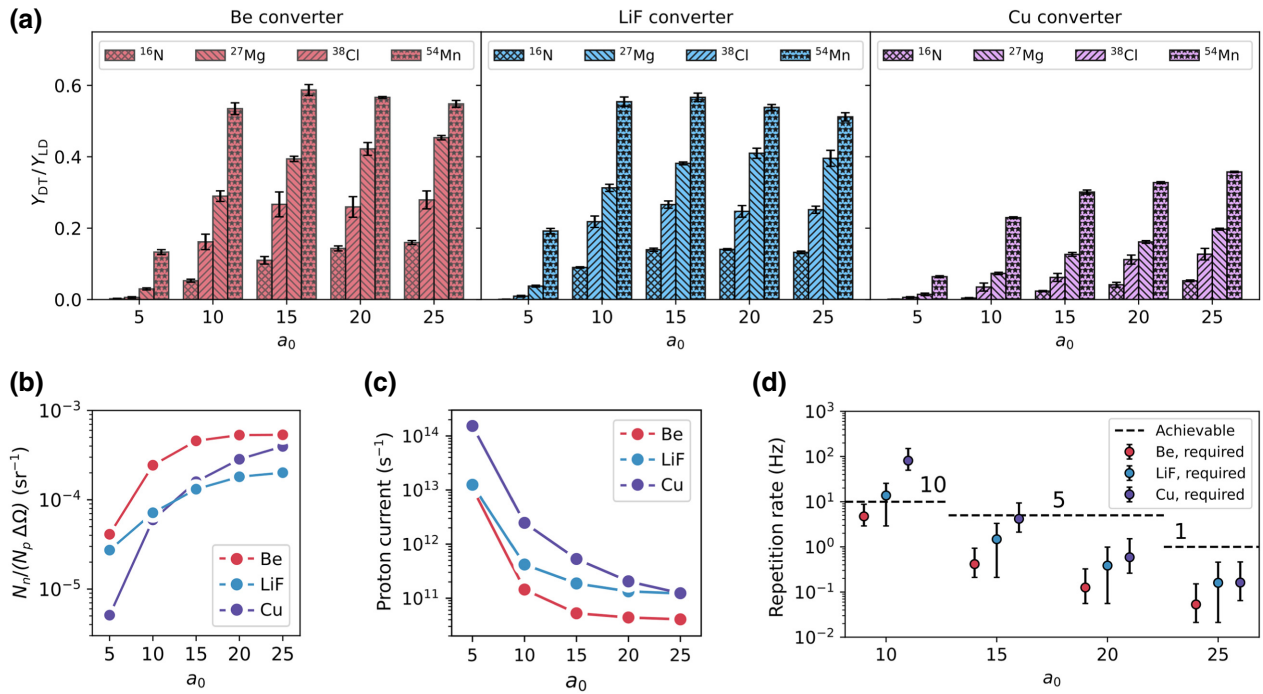
FIG. 3.   Monte Carlo results for the laser-driven FNAA feasibility assessment. (a) The ratio between the number of nuclear reactions achieved with the *D-T* generator and laser-driven sources. (b) Laser-driven neutrons emitted in the forward direction per unit of incident proton and solid angle. (c) Required laser-driven proton current to have the same neutron activation achieved with the *D-T* source. (d) Comparison between the required laser repetition rate (markers) and nominal values of commercial systems (dotted lines).

the main characteristic features of the cross sections. As far as laser-driven sources are concerned, protons are accelerated from the target almost instantaneously. Thus, the temporal spread of the neutron source is mainly related to the different times that nonmonoenergetic protons spend to reach and interact with the converter. In the MC simulations, we retrieve the instant of time at which neutrons leave the rear surface of the converter. The FWHM of the emission time distribution is reported in Fig. 4(b) as a function of a_0 for each converter material. It is lower than 1.2 ns for all the case studies considered here. Another parameter affecting the TOF resolution is the lateral dimension of the neutron source. Typically, it is of the order of some cm. We retrieve the radial position of neutrons at the rear surface of the converter, and we evaluate the source spot size as $2 \times$ FWHM of the distribution. As shown in Fig. 4(c), the spot size is always smaller than 1 cm. Therefore, the laser-driven source time and spatial spread are sufficiently small for pulsed FNRR.

As previously mentioned, the minimum neutron flux at the detector should be approximately 10^4 n/(cm^2 s). We aim to compare this value with the fluxes achieved with the laser-driven neutron sources. We evaluate the number of neutrons per unit of primary proton and solid angle emitted within $\pm5°$ to the converter normal direction and energies between 0.5 and 11 MeV. The yields are reported in Fig. 4(d). At a 3-m distance, the area subtended by the

corresponding solid angle is sufficiently wide to inspect large objects (approximately 50 cm lateral size), and the energy-angle distribution is uniform (see Appendix A). Then, by combining the yields with the number of protons accelerated per shot [from scaling Eq. (6)] and the nominal repetition rates, we obtain the fluxes delivered by the laser-driven neutron sources. They are compared with the minimum required neutron flux in Fig. 4(e). The analysis shows that DLTs and $a_0 = 20 - 25$ are necessary to perform pulsed FNRR with laser-driven sources exploiting commercial systems. Moreover, the highest neutron fluxes are provided by Be converters. Again, these conclusions are conservative concerning the number of protons, since the enhancement provided by DLTs is neglected. In addition, the neutron flux along the beam axis can be further enhanced via neutron collimation downstream of the converter [87]. We do not include this component in the analysis since its design is beyond the scope of this work.

It is well known that the proton spectrum is subject to a certain degree of fluctuation in terms of slope and cutoff energy during experiments. However, to achieve a reliable laser-driven FNRR analysis, the neutron spectrum shape must not vary from shot to shot. We assess this requirement by considering the $a_0 = 20$ and Be converter case study. For this specific condition, the proton spectrum provided to the MC simulation is modeled as Eq. (5), considering $T_e = 9$ MeV and $E_{p,\max} = 57.6$ MeV. Here, we perform four
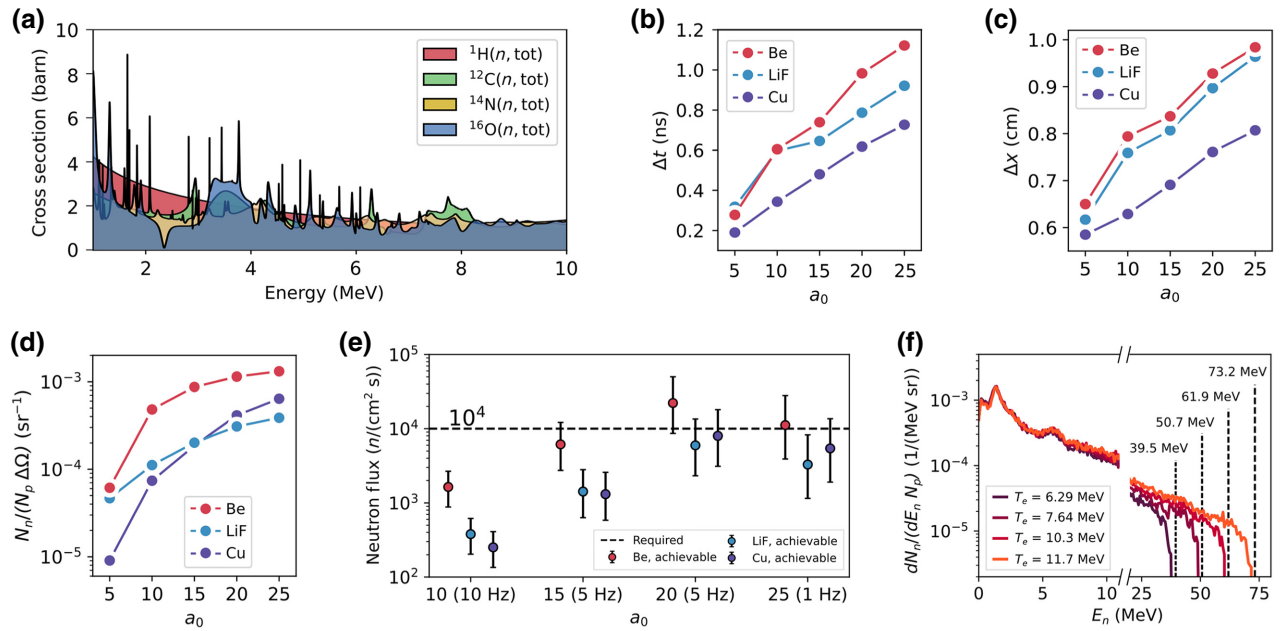
FIG. 4. Monte Carlo results for the laser-driven FNRR feasibility assessment. (a) Total neutron cross sections for H, ^{12}C, ^{14}N, and ^{16}O. (b) Time spread and (c) spot size of laser-driven sources. (d) The number of neutrons per proton and solid angle emitted within $\pm 5°$ and with energy in the range 0.5–11 MeV. (e) Neutron fluxes provided by laser-driven sources. The dashed line is the minimum neutron flux required for pulsed FNRR. (f) Neutron energy spectra obtained from MC simulations considering realistic oscillations on the proton energy spectrum slope (i.e., T_e) and maximum energy (i.e., dotted vertical lines).

MC simulations of neutron generation considering different proton energy spectra as input. They are defined by T_e = 6.3 7.6, 10.3, and 11.7 MeV, corresponding to deviations of ± 15 and $\pm 30\%$ from the original value. According to the model [47], the maximum proton energies are equal to 39.5, 50.7, 61.9, and 73.2 MeV. The neutron energy spectra retrieved from MC simulations are presented in Fig. 4(f). We consider neutrons emitted from the converter rear side and within a divergence angle of $\pm 5°$. As expected, the maximum neutron energies vary according to the cutoff energies of the incident protons. Nevertheless, the proton spectrum shape in the energy range of interest for pulsed FNRR (i.e., within 0–11 MeV) does not change. Therefore, we can conclude that shot-to-shot proton spectrum fluctuations will not affect the reliability of laser-driven FNRR.

E. Laser-driven FNRR simulated experiments

The last part of the work is devoted to the MC simulation of laser-driven FNRR analysis. The goal is to address whether elemental mapping can be effectively achieved. The simulation setup is presented in Fig. 5(a). We consider the best case study arising from the investigation presented in the previous section, namely $a_0 = 20$, 9 J laser energy, a repetition rate of 5 Hz and Be converter. Two samples are considered [see left column of Fig. 5(b)] having the external shape of a box, 12 cm wide and 5 cm deep. The

boxes, made of plastic $[(C_2H_4)_n]$ and steel, are crossed by cylinders containing water (H_2O) and methamphetamine $(C_{10}H_{15}N)$. Therefore, we study three materials with elements sensitive to the technique and one that does not. Moreover, one of the substances (i.e., the $C_{10}H_{15}N$) is often used as a recreational drug. The identification of its constituents is within the scopes of pulsed FNRR. Samples are placed 3 m far from the laser-driven neutron source (i.e., the rear side of the converter). A detector screen is located 3.5 m from the source. Between the sample and detector, we place a 3-mm lead plate. Its role during an experiment is to screen the detector from the flash radiation emitted during the laser-target interaction [37].

We perform two MC simulations with the samples (one for each) and one simulation without samples. Primary particles are neutrons having energies and angular divergence extracted from the distribution presented in Fig. 1(f). The angular divergence is limited between $\pm 2°$ to avoid simulating unnecessary events. The initial position of each neutron (in the plane orthogonal to the beam) is sampled from the radial distribution (FWHM = 9.3 mm) obtained in previous simulations. Therefore, the actual size of the source is taken into account. Then, the arrival time and position of neutrons reaching the detector screen are retrieved. We also include the uncertainty of the emission time of neutrons from the source in the simulation. Indeed, for each arrival time, we apply a time shift extracted from the time spread distribution (FWHM = 1 ns). Moreover, the
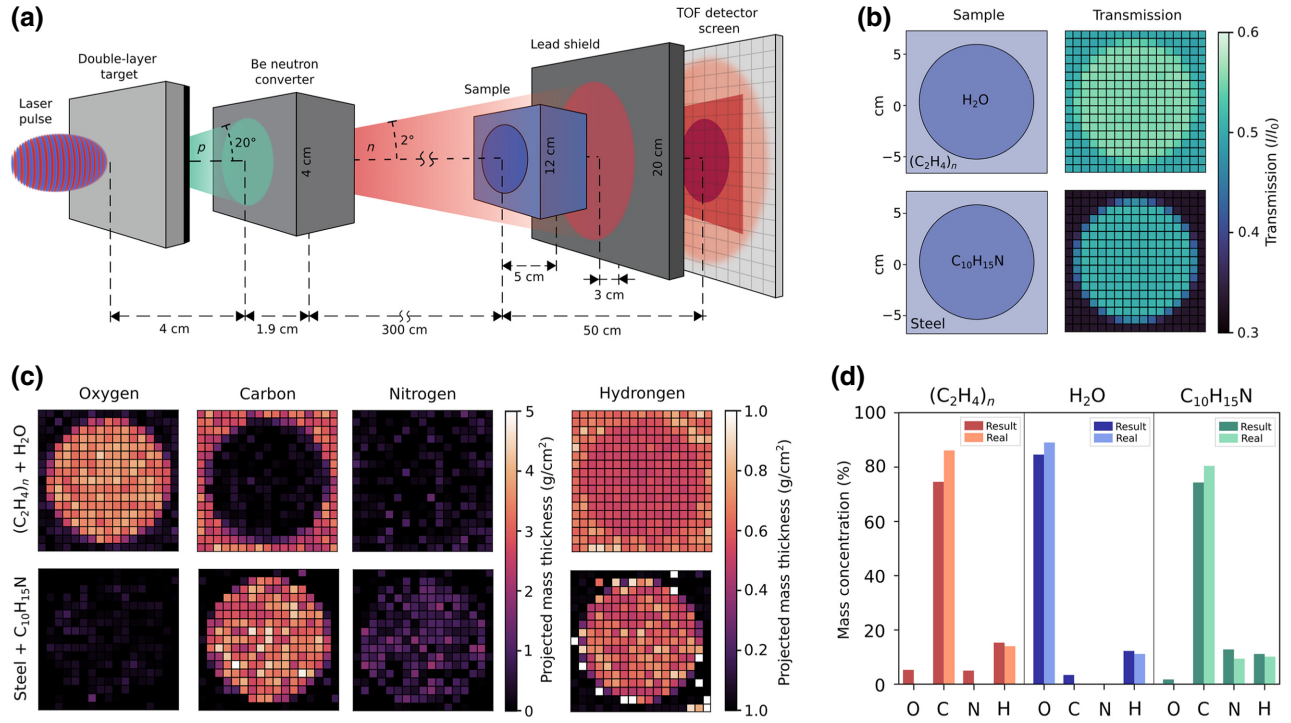
FIG. 5. Monte Carlo results for the laser-driven FNRR simulated experiments. (a) Monte Carlo simulation setup. (b) Composition between the samples and maps of the total neutron transmission. (c) Maps of the projected mass thickness of the elements (columns) for the two samples (rows). (d) Retrieved and original (i.e., set in the MC) mass concentrations of the elements in the materials.

arrival times are collected considering 1-ns spaced time bins. It is coherent with the time resolution of available detectors [38].

For each simulation, we perform several runs representing single-laser shots. Then, the data obtained from every run are merged. Indeed, we have an average number of protons per shot equal to 3.4×10^{11} [from scaling (6)]. Since the neutron yield per unit solid angle is 1.2×10^{-3} sr^{-1} and we consider particles within $\pm 2°$ to the beam direction, the average number of neutrons simulated in each run is 1.6×10^6. Thus, we perform 300 runs (i.e., shots) for each simulation to achieve the typical irradiation condition for pulsed FNRR (i.e., approximately 10^{11} n/sr [37,38,44]). Note that, working at the nominal repetition rate of 5 Hz, the corresponding measurement would last 60 seconds. As already mentioned, the number of accelerated protons is subject to a certain degree of shot-to-shot uncertainty. To take this aspect into account in the simulations as well, we sample the number of neutrons for each run from a Gaussian distribution centered on 1.6×10^6 and with a standard deviation of 0.47×10^6 (corresponding to an uncertainty of about 30% on the accelerated number of protons). Further details about MC simulations are provided in Appendix A.

From the detection of the arrival times of neutrons at the detector (i.e., TOF), we retrieve their energies. Then, by performing the ratio between the number of neutrons

reaching the detector screen in the presence $I(E_n)$ and the absence $I_0(E_n)$ of samples, we obtain the transmission $I(E_n)/I_0(E_n)$ in each pixel. The integrals over E_n for both samples are shown in the right column of Fig. 5(b). This measurement corresponds to conventional neutron imaging where all neutrons are detected, and no energy discrimination is performed. The presence of four distinct materials, and their spatial distribution, can be distinguished. However, no information about the elemental composition is achieved. To this aim, we must solve the following equation for every pixel:

$$\frac{I(E_n)}{I_0(E_n)} - \exp\left(-N_{Av} \sum_i \sigma_i(E_n) \frac{r_i}{M_i} - \Gamma\right) - C(E_n) = 0, \qquad (19)$$

where the i index identifies the C, N, O, and H elements, σ_i are the total cross sections, r_i are the projected elemental mass thicknesses, M_i are the atomic masses, Γ describes transmission through other materials, and $C(E_n)$ is an energy-dependent function accounting for neutron scattering. For a detailed description of $C(E_n)$ and the overall procedure to solve Eq. (19), see Appendix B.

The solutions r_i are reported in Fig. 5(c). Remarkably, we can reconstruct the distribution of the elements over the surfaces of the samples. Starting from the heavier elements

(i.e., O, C, and N), oxygen is only detected where water is contained, while the presence of carbon is highlighted for plastic and methamphetamine. Nitrogen is identified in the region corresponding to the cylinder filled with $C_{10}H_{15}N$, even if present in low concentration. As far as hydrogen is concerned, we can appreciate its different concentrations in plastic and water, as well as its presence in methamphetamine. Correctly, none of the elements considered is identified for steel. Note that there are pixels for which small amounts of elements not actually present are detected, especially for N and H. They are due to the unavoidable error associated with the finite number of neutrons and to the sources of uncertainty we introduce in the simulations (e.g., spatial and time spread, neutron number fluctuation, and TOF binning). However, they are randomly distributed over the entire detector screen since they are not due to the presence of a specific element. As a consequence, they can be correctly recognized as a background.

As a final step, we can perform the average of $I(E_n)/I_0(E_n)$ over pixels associated with the same material [from the total attenuation in Fig. 5(b)] and solve Eq. (19). We perform the ratio $r_i / \sum_i r_i$ for each element and material to retrieve the average elemental concentrations for O, C, N, and H in plastic, water, and methamphetamine. The results are compared with the actual concentrations in Fig. 5(d). The agreement is satisfactory for all the elements and materials. This result, in conjunction with the mapping of the elements, suggests that the proposed laser-driven source could be exploited for pulsed FNRR.

III. CONCLUSIONS

Laser-driven radiation sources are appealing solutions for materials analysis and inspection. They can provide ions, electrons, photons, and neutrons in a broad range of energies. In conjunction with other applications foreseen for compact laser-driven sources in the field of materials characterization (e.g., PIXE, EDX, imaging), the development of laser-driven FNAA and FNRR represents a further step toward the realization of a multifunctional setup for materials analysis and inspection.

In this work, we investigate the generation of fast neutrons exploiting 10s fs, 1–15 J energy commercial lasers and advanced DLTs, as well as their use for FNAA and FNRR via MC simulations. We study neutron generation from laser-driven protons in a pitcher-catcher configuration, considering a broad range of laser intensities and various converter materials. We provide analytical relations to estimate the neutron yields with bare targets and DLTs. Then, for the main case studies, we address the feasibility of laser-driven FNRR and FNAA in terms of achievable neutron fluxes and stability of the source. To satisfy the requirements for the techniques, the use of

DLTs is mandatory. Lastly, we fully simulated a laser-driven FNRR experiment to assess whether the elemental distribution of low-Z elements is feasible. Based on these results we can conclude that laser-driven FNAA and FNRR can be achieved with performances comparable to those obtained with D-T generators and particle accelerators. To this aim, the commercially available lasers (i.e., intensity $I \geq 10^{20}$ W/cm^2, time duration approximately 30 fs, and energy approximately 1–15 J) working at a high repetition rate (i.e., 1–10 Hz) are suitable. It is worth mentioning that coupling commercial lasers and DLTs could also be exploited for applications involving epithermal and thermal neutrons.

APPENDIX A: MONTE CARLO SIMULATIONS

We perform several Geant4 MC simulations of neutron generation from (p, xn) reactions and propagation in the matter. To this aim, the hadronic processes are taken into account with the `G4HadronPhysicsQGSP_BIC_AllHP` physics list. It is the most reliable for (p, xn) reactions according to benchmarks performed in previous works [10,88,89]. Cross sections are derived from the TENDL-2014 and ENDFB-VII.1 data libraries. Several (p, xn) nuclear reactions take place involving different isotopes of the same element. The total cross sections $\sigma(E_p)$ for the converters are given by the combination of $\sigma(E_p)$ for each isotope and the relative isotopic abundances. Figure 6 reports the total neutron production cross sections of interest for the aims of this work.

Electromagnetic processes involving primary protons and secondary charged particles are modeled via the `G4EmStandardPhysics_option3` module. We also activate the `G4RadioactiveDecayPhysics` physics
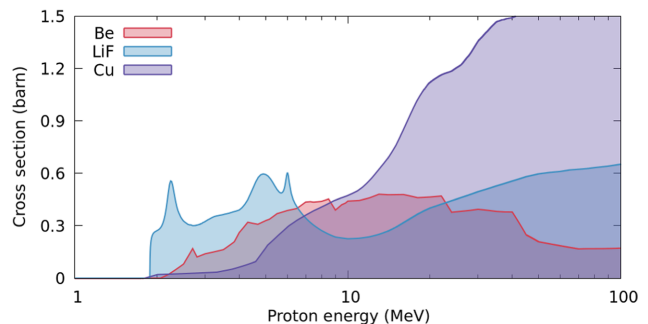

FIG. 6.   Total (p, xn) cross sections for Be, LiF, and Cu converters from the TENDL-2014 and ENDFB-VII.1 data libraries.
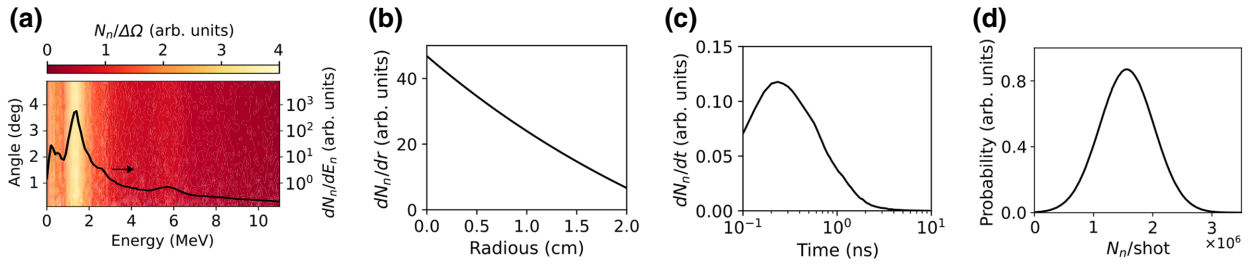
FIG. 7.   Input distributions for the laser-driven FNRR simulations. (a) Color map of the energy-angle distribution between $0°$–$5°$ and 0–11 MeV. The black line is the energy distribution, and the arrow points to the corresponding y axis. (b) Radial distribution of neutrons emitted from the converter surface. (c) Distribution of neutron emission time from the converter surface. (d) Distribution of the number of neutrons emitted within $\pm 2°$ divergence angle per laser shot.

list. The production cuts for secondary particles are set equal to 10 µm. As mentioned in the main text, several MC simulations (i.e., runs) have been performed in parallel by setting different seeds for the pseudorandom number generator (PNG), and the final results are aggregated. To this aim, we exploit the HepJamesRandom generator, which applies the Marsaglia-Zaman RANMAR algorithm [90]. It provides long sequences (i.e., approximately 10^9) of independent random numbers.

Specifically, the neutron yields and energy spectra presented in Figs. 1(c)–1(f) are obtained with 30 MC simulations (i.e., for single-layers and DLTs, five values of a_0, and three converter materials) with 3×10^7 primary protons for each. The corresponding MC simulations are carried out with approximately 10^9 primary protons to resolve adequately the energy-angle distributions in Figs. 1(g)–1(i). As far as the influence of the proton

spectrum fluctuation is concerned, the results presented in Fig. 4(f) are obtained with 3×10^7 primary protons for each MC simulation.

In the laser-driven FNRR simulations, primary neutrons are emitted along the beam axis (i.e., $\pm 2°$) and $E_n <$ 11 MeV. The energy-angle distribution within these intervals must be properly addressed in advance. Therefore, we perform a simulation of neutron generation from Be converter, $a_0 = 20$ and DLT proton spectrum with approximately 10^9 primary particles, exploiting cross-section biasing to enhance the neutron generation by 2 orders of magnitude. The resulting energy-angle distribution normalized to the solid angle is reported in Fig. 7(a). It is uniform in the divergence angle. The proton energy distribution, integrated between $0°$ and $5°$, is superimposed on the color map. In the laser-driven FNRR simulation, primary neutron energies and divergence angles are sampled
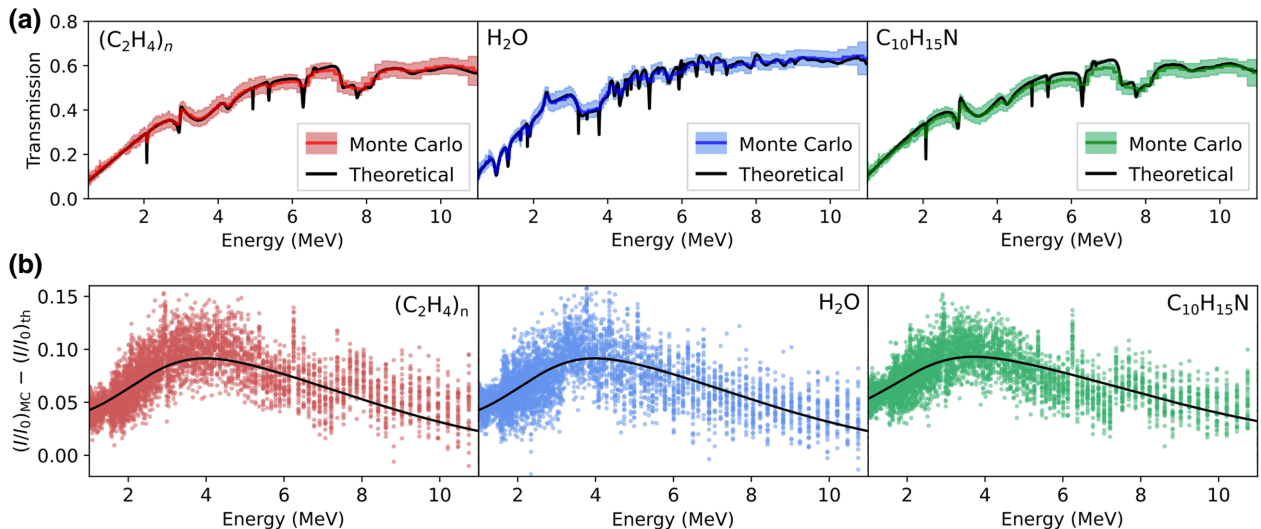

FIG. 8.   Model implementation for the pulsed FNRR elemental imaging reconstruction. (a) Comparison between the neutron transmission from MC simulation (colored line) and retrieved with the least-squares procedure (the black lines). The colored bands represent the statistical uncertainty (i.e., $\pm$ standard deviation) performed over the pixels from the MC simulations. (b) Neutron scattering contribution to the transmission. Colored points are the difference between transmissions from MC simulations and the expected theoretical ones. The black lines are the fits with the asymmetric Gaussian function.

from these distributions with the inverse transform sampling method. The same procedure is applied to extract the primary neutron radial positions, time spread, and the number of simulated particles for each run from the distributions reported in Figs. 8(b)–8(d), respectively.

APPENDIX B: DETAILS OF THE RECONSTRUCTION METHOD FOR PULSED FNRR

As already mentioned, Eq. (19) must be solved to retrieve the projected mass thicknesses r_i for C, N, O, and H. The solution is found by exploiting a least-squares minimization procedure. For each pixel, the values of r_i that provide the best agreement between the simulated transmission and the theoretical one are obtained. During the iteration procedure, the values of r_i are positively constrained.

The comparisons between the retrieved and simulated neutron transmission for plastic, water, and $C_{10}H_{15}N$ are presented in Fig. 8. They take into account the contribution from scattered neutrons interacting with other pixels. This contribution is modeled with an asymmetric Gaussian function:

$$C(E_n) = \frac{C_0}{C_2\sqrt{2\pi}} \exp\left(-\frac{-(E_n - C1)^2}{2C_2^2}\right)$$
$$\times \left(1 + \text{erfc}\left(\frac{C_3(E_n - C_1)}{C_2\sqrt{2}}\right)\right). \quad \text{(B1)}$$

In Fig. 8(b), the difference between the transmission from MC simulation in each pixel and the expected one (net of scattering contributions) is reported as colored points. The black lines represent the fit performed with the asymmetric Gaussian Eq. (B1). Overall, the selected energy dependence for $C(E_n)$ well fits the scattering contribution for all materials. As expected, it is always positive since neutrons scattered on the screen can only increase the attenuated neutron flux in the pixels.

[1] A. Macchi, M. Borghesi, and M. Passoni, Ion acceleration by superintense laser-plasma interaction, Rev. Mod. Phys. **85**, 751 (2013).

[2] H. Daido, M. Nishiuchi, and A. S. Pirozhkov, Review of laser-driven ion sources and their applications, Rep. Prog. Phys. **75**, 056401 (2012).

[3] C. N. Danson, C. Haefner, J. Bromage, T. Butcher, J.-C. F. Chanteloup, E. A. Chowdhury, A. Galvanauskas, L. A. Gizzi, J. Hein, D. I. Hillier, *et al.*, Petawatt and exawatt class lasers worldwide, High Power Laser Sci. Eng. 7, e54 (2019).

[4] I. Prencipe, J. Fuchs, S. Pascarelli, D. Schumacher, R. Stephens, N. Alexander, R. Briggs, M. Büscher, M. Cernaianu, A. Choukourov, *et al.*, Targets for high repetition rate laser facilities: Needs, challenges and perspectives, High Power Laser Sci. Eng. **5**, e17 (2017).

[5] M. Passoni, A. Sgattoni, I. Prencipe, L. Fedeli, D. Dellasega, L. Cialfi, I. W. Choi, I. J. Kim, K. A. Janulewicz, H. W. Lee, *et al.*, Toward high-energy laser-driven ion beams: Nanostructured double-layer targets, Phys. Rev. Accel. Beams **19**, 061301 (2016).

[6] I. Prencipe, A. Sgattoni, D. Dellasega, L. Fedeli, L. Cialfi, I. W. Choi, I. J. Kim, K. A. Janulewicz, K. Kakolee, H. W. Lee, *et al.*, Development of foam-based layered targets for laser-driven ion beam production, Plasma Phys. Controlled Fusion **58**, 034019 (2016).

[7] J. Bin, M. Yeung, Z. Gong, H. Wang, C. Kreuzer, M. Zhou, M. Streeter, P. Foster, S. Cousens, B. Dromey, *et al.*, Enhanced Laser-Driven Ion Acceleration by Superponderomotive Electrons Generated from Near-Critical-Density Plasma, Phys. Rev. Lett. **120**, 074801 (2018).

[8] M. Passoni, A. Zani, A. Sgattoni, D. Dellasega, A. Macchi, I. Prencipe, V. Floquet, P. Martin, T. Liseykina, and T. Ceccotti, Energetic ions at moderate laser intensities using foam-based multi-layered targets, Plasma Phys. Controlled Fusion **56**, 045001 (2014).

[9] I. Prencipe, J. Metzkes-Ng, A. Pazzaglia, C. Bernert, D. Dellasega, L. Fedeli, A. Formenti, M. Garten, T. Kluge, S. Kraft, *et al.*, Efficient laser-driven proton and bremsstrahlung generation from cluster-assembled foam targets, New J. Phys. **23**, 093015 (2021).

[10] L. Fedeli, A. Formenti, A. Pazzaglia, F. M. Arioli, A. Tentori, and M. Passoni, Enhanced laser-driven hadron sources with nanostructured double-layer targets, New J. Phys. **22**, 033045 (2020).

[11] O. Rosmej, N. Andreev, S. Zaehter, N. Zahn, P. Christ, B. Borm, T. Radon, A. Sokolov, L. Pugachev, D. Khaghani, *et al.*, Interaction of relativistically intense laser pulses with long-scale near critical plasmas for optimization of laser based sources of MeV electrons and gamma-rays, New J. Phys. **21**, 043044 (2019).

[12] O. Rosmej, M. Gyrdymov, M. Günther, N. Andreev, P. Tavana, P. Neumayer, S. Zähter, N. Zahn, V. Popov, N. Borisenko, *et al.*, High-current laser-driven beams of relativistic electrons for high energy density research, Plasma Phys. Controlled Fusion **62**, 115024 (2020).

[13] G. Sarri, W. Schumaker, A. Di Piazza, M. Vargas, B. Dromey, M. E. Dieckmann, V. Chvykov, A. Maksimchuk, V. Yanovsky, Z. He, *et al.*, Table-Top Laser-Based Source of Femtosecond, Collimated, Ultrarelativistic Positron Beams, Phys. Rev. Lett. **110**, 255002 (2013).

[14] A. Alejo, H. Ahmed, A. Green, S. Mirfayzi, M. Borghesi, and S. Kar, Recent advances in laser-driven neutron sources, Il Nuovo Cimento C **38**, 1 (2015).

[15] M. Günther, O. Rosmej, P. Tavana, M. Gyrdymov, A. Skobliakov, A. Kantsyrev, S. Zähter, N. Borisenko, A. Pukhov, and N. Andreev, Forward-looking insights in laser-generated ultra-intense γ-ray and neutron sources for nuclear application and science, Nat. Commun. **13**, 1 (2022).

[16] M. Barberio, S. Veltri, M. Sciscià, and P. Antici, Laser-accelerated proton beams as diagnostics for cultural heritage, Sci. Rep. **7**, 40415 (2017).

[17] M. Passoni, L. Fedeli, and F. Mirani, Superintense laser-driven ion beam analysis, Sci. Rep. **9**, 1 (2019).

[18] F. Mirani, A. Maffini, F. Casamichiela, A. Pazzaglia, A. Formenti, D. Dellasega, V. Russo, D. Vavassori, D. Bortot, M. Huault, *et al.*, Integrated quantitative PIXE analysis and EDX spectroscopy using a laser-driven particle source, Sci. Adv. **7**, eabc8660 (2021).

[19] P. Puyuelo-Valdes, S. Vallières, M. Salvadori, S. Fourmaux, S. Payeur, J.-C. Kieffer, F. Hannachi, and P. Antici, Combined laser-based x-ray fluorescence and particle-induced x-ray emission for versatile multi-element analysis, Sci. Rep. **11**, 1 (2021).

[20] M. Passoni, F. Arioli, L. Cialfi, D. Dellasega, L. Fedeli, A. Formenti, A. Giovannelli, A. Maffini, F. Mirani, A. Pazzaglia, *et al.*, Advanced laser-driven ion sources and their applications in materials and nuclear science, Plasma Phys. Controlled Fusion **62**, 014022 (2019).

[21] F. Valle Brozas, A. Crego, L. Roso, and A. Peralta Conde, Laser-based x-ray and electron source for x-ray fluorescence studies, Appl. Phys. B **122**, 1 (2016).

[22] T. L. Audet, A. Alejo, L. Calvin, M. H. Cunningham, G. R. Frazer, G. Nersisyan, M. Phipps, J. R. Warwick, G. Sarri, N. A. Hafz, *et al.*, Ultrashort, MeV-scale laser-plasma positron source for positron annihilation lifetime spectroscopy, Phys. Rev. Accel. Beams **24**, 073402 (2021).

[23] F. Mirani, D. Calzolari, A. Formenti, and M. Passoni, Superintense laser-driven photon activation analysis, Commun. Phys. **4**, 1 (2021).

[24] M. Roth, D. Jung, K. Falk, N. Guler, O. Deppert, M. Devlin, A. Favalli, J. Fernandez, D. Gautier, M. Geissel, *et al.*, Bright Laser-Driven Neutron Source Based on the Relativistic Transparency of Solids, Phys. Rev. Lett. **110**, 044802 (2013).

[25] I. Pomerantz, E. Mccary, A. R. Meadows, A. Arefiev, A. C. Bernstein, C. Chester, J. Cortez, M. E. Donovan, G. Dyer, E. W. Gaul, *et al.*, Ultrashort Pulsed Neutron Source, Phys. Rev. Lett. **113**, 184801 (2014).

[26] J. Feng, C. Fu, Y. Li, X. Zhang, J. Wang, D. Li, C. Zhu, J. Tan, M. Mirzaie, Z. Zhang, *et al.*, High-efficiency neutron source generation from photonuclear reactions driven by laser plasma accelerator, High Energy Density Phys. **36**, 100753 (2020).

[27] D. Hilscher, O. Berndt, M. Enke, U. Jahnke, P. Nickles, H. Ruhl, and W. Sandner, Neutron energy spectra from the laser-induced D$(d, n)^3$ He reaction, Phys. Rev. E **64**, 016414 (2001).

[28] A. Alejo, A. Krygier, H. Ahmed, J. Morrison, R. Clarke, J. Fuchs, A. Green, J. Green, D. Jung, A. Kleinschmidt, *et al.*, High flux, beamed neutron sources employing deuteron-rich ion beams from D$_2$O-ice layered targets, Plasma Phys. Controlled Fusion **59**, 064004 (2017).

[29] A. Kleinschmidt, V. Bagnoud, O. Deppert, A. Favalli, S. Frydrych, J. Hornung, D. Jahn, G. Schaumann, A. Tebartz, F. Wagner, *et al.*, Intense, directed neutron beams from a laser-driven neutron source at phelix, Phys. Plasmas **25**, 053101 (2018).

[30] D. Higginson, J. McNaney, D. Swift, T. Bartal, D. Hey, R. Kodama, S. Le Pape, A. Mackinnon, D. Mariscal, H. Nakamura, *et al.*, Laser generated neutron source for neutron resonance spectroscopy, Phys. Plasmas **17**, 100701 (2010).

[31] S. R. Mirfayzi, A. Alejo, H. Ahmed, D. Raspino, S. Ansell, L. A. Wilson, C. Armstrong, N. M. Butler, R. Clarke, A. Higginson, *et al.*, Experimental demonstration of a compact epithermal neutron source based on a high power laser, Appl. Phys. Lett. **111**, 044101 (2017).

[32] C. Brenner, S. Mirfayzi, D. Rusby, C. Armstrong, A. Alejo, L. Wilson, R. Clarke, H. Ahmed, N. Butler, D. Haddock, *et al.*, Laser-driven x-ray and neutron source development for industrial applications of plasma accelerators, Plasma Phys. Controlled Fusion **58**, 014039 (2015).

[33] C. P. Jones, C. M. Brenner, C. A. Stitt, C. Armstrong, D. R. Rusby, S. R. Mirfayzi, L. A. Wilson, A. Alejo, H. Ahmed, R. Allott, *et al.*, Evaluating laser-driven bremsstrahlung radiation sources for imaging and analysis of nuclear waste packages, J. Hazard. Mater. **318**, 694 (2016).

[34] S. Chen, F. Negoita, K. Spohr, E. d'Humières, I. Pomerantz, and J. Fuchs, Extreme brightness laser-based neutron pulses as a pathway for investigating nucleosynthesis in the laboratory, Matter Rad. Extremes **4**, 054402 (2019).

[35] M. Zimmer, S. Scheuren, A. Kleinschmidt, N. Mitura, A. Tebartz, G. Schaumann, T. Abel, T. Ebert, M. Hesse, Ş. Zähter, *et al.*, Demonstration of non-destructive and isotope-sensitive material analysis using a short-pulsed laser-driven epi-thermal neutron source, Nat. Commun. **13**, 1 (2022).

[36] S. Lee, S. Park, K. Lee, and H. Cha, A laser-induced repetitive fast neutron source applied for gold activation analysis, Rev. Sci. Instrum. **83**, 123504 (2012).

[37] I. Kishon, A. Kleinschmidt, V. Schanz, A. Tebartz, O. Noam, J. Fernandez, D. Gautier, R. Johnson, T. Shimada, G. Wurden, *et al.*, Laser based neutron spectroscopy, Nucl. Instrum. Methods Phys. Res. Sect. A: Accelerators, Spectrometers, Detectors and Associated Equip. **932**, 27 (2019).

[38] O. Noam, D. C. Gautier, N. Fotiades, A. Beck, and I. Pomerantz, Fast neutron resonance radiography with full time-series digitization, Nucl. Instrum. Methods Phys. Res. Sect. A: Accelerators, Spectrometers, Detectors and Associated Equip. **955**, 163309 (2020).

[39] A. Vinković, J. Obhođaš, D. Sudac, K. Nađ, and V. Valković, Analysis of carbon in sediments using fast neutron activation analysis (FNAA), J. Soils Sediments **20**, 2741 (2020).

[40] N. Marchese, A. Cannuli, M. Caccamo, and C. Pace, New generation non-stationary portable neutron generators for biophysical applications of neutron activation analysis, Biochim. et Biophys. Acta (BBA)-Gen. Subjects **1861**, 3661 (2017).

[41] F. Mildenberger and E. Mauerhofer, Cyclic neutron activation analysis of large samples with a pulsed 14 mev neutron source, J. Radioanal. Nucl. Chem. **311**, 917 (2017).

[42] E. Witkowska, K. Szczepaniak, and M. Biziuk, Some applications of neutron activation analysis, J. Radioanal. Nucl. Chem. **265**, 141 (2005).

[43] V. Dangendorf, G. Laczko, C. Kersten, O. Jagutzki, and U. Spillmann, Fast neutron resonance radiography in a pulsed neutron beam, (2003), arXiv preprint ArXiv:nucl-ex/0301001.

[44] D. Perticone, B. W. Blackburn, G. Chen, W. A. Franklin, E. E. Ihloff, G. E. Kohse, R. C. Lanza, B. McAllister,

and V. Ziskin, Fast neutron resonance radiography for elemental imaging, Nucl. Instrum. Methods Phys. Res. Sect. A: Accelerators, Spectrometers, Detectors and Associated Equip. **922,** 71 (2019).

[45] D. Vartsky, in *International Workshop on Fast Neutron Detectors and Applications*, Vol. 25 (SISSA Medialab, 2007), p. 084.

[46] V. Hornỳ, S. N. Chen, X. Davoine, V. Lelasseux, L. Gremillet, and J. Fuchs, High-flux neutron generation by laser-accelerated ions from single- and double-layer targets, Sci. Rep. **12,** 19767 (2022).

[47] A. Pazzaglia, L. Fedeli, A. Formenti, A. Maffini, and M. Passoni, A theoretical model of laser-driven ion acceleration from near-critical double-layer targets, Commun. Phys. **3,** 1 (2020).

[48] J. Allison, K. Amako, J. Apostolakis, P. Arce, M. Asai, T. Aso, E. Bagli, A. Bagulya, S. Banerjee, G. Barrand, *et al.*, Recent developments in Geant4, Nucl. Instrum. Methods Phys. Res. Sect. A: Accelerators, Spectrometers, Detectors and Associated Equip. **835,** 186 (2016).

[49] J. Allison, K. Amako, J. Apostolakis, H. Araujo, P. A. Dubois, M. Asai, G. Barrand, R. Capra, S. Chauvie, R. Chytracek, *et al.*, Geant4 developments and applications, IEEE Trans. Nucl. Sci. **53,** 270 (2006).

[50] A. Zani, D. Dellasega, V. Russo, and M. Passoni, Ultra-low density carbon foams produced by pulsed laser deposition, Carbon **56,** 358 (2013).

[51] A. Maffini, A. Pazzaglia, D. Dellasega, V. Russo, and M. Passoni, Growth dynamics of pulsed laser deposited nanofoams, Phys. Rev. Mater. **3,** 083404 (2019).

[52] A. Maffini, D. Orecchia, A. Pazzaglia, M. Zavelani-Rossi, and M. Passoni, Pulsed laser deposition of carbon nanofoam, Appl. Surf. Sci. **599,** 153859 (2022).

[53] W. Ma, L. Song, R. Yang, T. Zhang, Y. Zhao, L. Sun, Y. Ren, D. Liu, L. Liu, J. Shen, *et al.*, Directly synthesized strong, highly conducting, transparent single-walled carbon nanotube films, Nano Lett. **7,** 2307 (2007).

[54] *QUARK 200/350/500: Ultrafast Ti:Sa Laser Series*, Thales, https://perma.cc/48HH-GYG6 Accessed: 2023-03-12.

[55] *Pulsar TW: Ultra intense ultrafast laser*, Amplitude Technologies, https://perma.cc/3K44-N7CV Accessed: 2023-03-12.

[56] M. Zimmer, S. Scheuren, T. Ebert, G. Schaumann, C. Rödel, M. Roth, B. Schmitz, V. Bagnoud, and J. Hornung, Analysis of laser-proton acceleration experiments for development of empirical scaling laws, Phys. Rev. E **104,** 045210 (2021).

[57] J. Bin, W. Ma, H. Wang, M. Streeter, C. Kreuzer, D. Kiefer, M. Yeung, S. Cousens, P. Foster, B. Dromey, *et al.*, Ion Acceleration Using Relativistic Pulse Shaping in Near-Critical-Density Plasmas, Phys. Rev. Lett. **115,** 064801 (2015).

[58] W. Ma, I. J. Kim, J. Yu, I. W. Choi, P. Singh, H. W. Lee, J. H. Sung, S. K. Lee, C. Lin, Q. Liao, *et al.*, Laser Acceleration of Highly Energetic Carbon Ions Using a Double-Layer Target Composed of Slightly Underdense Plasma and Ultrathin Foil, Phys. Rev. Lett. **122,** 014803 (2019).

[59] P. Mora, Plasma Expansion into a Vacuum, Phys. Rev. Lett. **90,** 185002 (2003).

[60] A. Formenti, A. Maffini, and M. Passoni, Non-equilibrium effects in a relativistic plasma sheath model, New J. Phys. **22,** 053020 (2020).

[61] S. Fritzler, V. Malka, G. Grillon, J.-P. Rousseau, F. Burgy, E. Lefebvre, E. d'Humieres, P. McKenna, and K. Ledingham, Proton beams generated with high-intensity lasers: Applications to medical isotope production, Appl. Phys. Lett. **83,** 3039 (2003).

[62] Q. Liao, M. Wu, Z. Gong, Y. Geng, X. Xu, D. Li, Y. Shou, J. Zhu, C. Li, M. Yang, *et al.*, Enhanced laser proton acceleration by target ablation on a femtosecond laser system, Phys. Plasmas **25,** 063109 (2018).

[63] D. Li, T. Yang, M. Wu, H. Cheng, Y. Li, Y. Xia, Y. Yan, Y. Geng, Y. Zhao, C. Lin, *et al.*, Manipulation of laser-accelerated proton beam spatial distribution by laser machined microstructure targets, Phys. Plasmas **28,** 113101 (2021).

[64] D. Zhou, D. Li, Y. Chen, M. Wu, T. Yang, H. Cheng, Y. Li, Y. Chen, Y. Li, Y. Geng, *et al.*, Preparation of graphene on SiC by laser-accelerated pulsed ion beams, Chin. Phys. B **30,** 116106 (2021).

[65] Y. Fang, X. Ge, S. Yang, W. Wei, T. Yu, F. Liu, M. Chen, J. Liu, X. Yuan, Z. Sheng, *et al.*, Different effects of laser contrast on proton emission from normal large foils and transverse-size-reduced targets, Plasma Phys. Controlled Fusion **58,** 075010 (2016).

[66] M. Nishiuchi, H. Daido, A. Yogo, S. Orimo, K. Ogura, J. Ma, A. Sagisaka, M. Mori, A. Pirozhkov, H. Kiriyama, *et al.*, Efficient production of a collimated MeV proton beam from a polyimide target driven by an intense femtosecond laser pulse, Phys. Plasmas **15,** 053104 (2008).

[67] M. Scisciò, E. d'Humières, S. Fourmaux, J. Kieffer, L. Palumbo, and P. Antici, Bidimensional particle-in-cell simulations for laser-driven proton acceleration using ultra-short, ultra-high contrast laser, Phys. Plasmas **21,** 123104 (2014).

[68] X. Xu, Q. Liao, M. Wu, Y. Geng, D. Li, J. Zhu, C. Li, R. Hu, Y. Shou, Y. Chen, *et al.*, Detection and analysis of laser driven proton beams by calibrated gafchromic HD-V2 and MD-V3 radiochromic films, Rev. Sci. Instrum. **90,** 033306 (2019).

[69] Y.-X. Geng, Y.-R. Shou, J.-G. Zhu, X.-H. Xu, M.-J. Wu, P.-J. Wang, D.-Y. Li, R.-H. Hu, D.-H. Wang, Y.-Y. Zhao, *et al.*, Generating proton beams exceeding 10 MeV using high contrast 60TW laser, Chin. Phys. Lett. **35,** 092901 (2018).

[70] L. Obst, S. Göde, M. Rehwald, F.-E. Brack, J. Branco, S. Bock, M. Bussmann, T. E. Cowan, C. B. Curry, F. Fiuza, *et al.*, Efficient laser-driven proton acceleration from cylindrical and planar cryogenic hydrogen jets, Sci. Rep. **7,** 1 (2017).

[71] P. L. Poole, L. Obst, G. E. Cochran, J. Metzkes, H.-P. Schlenvoigt, I. Prencipe, T. Kluge, T. Cowan, U. Schramm, D. W. Schumacher, *et al.*, Laser-driven ion acceleration via target normal sheath acceleration in the relativistic transparency regime, New J. Phys. **20,** 013019 (2018).

[72] S. Kar, H. Ahmed, R. Prasad, M. Cerchez, S. Brauckmann, B. Aurand, G. Cantono, P. Hadjisolomou, C. L. Lewis, A. Macchi, *et al.*, Guided post-acceleration of laser-driven ions by a miniature modular structure, Nat. Commun. **7,** 1 (2016).

[73] U. Masood, M. Bussmann, T. Cowan, W. Enghardt, L. Karsch, F. Kroll, U. Schramm, and J. Pawelke, A compact solution for ion beam therapy with laser accelerated protons, Appl. Phys. B **117**, 41 (2014).

[74] A. Mackinnon, Y. Sentoku, P. Patel, D. Price, S. Hatchett, M. Key, C. Andersen, R. Snavely, and R. Freeman, Enhancement of Proton Acceleration by Hot-Electron Recirculation in Thin Foils Irradiated by Ultraintense Laser Pulses, Phys. Rev. Lett. **88**, 215006 (2002).

[75] R. Prasad, S. Ter-Avetisyan, D. Doria, K. Quinn, L. Romagnani, P. Foster, C. Brenner, J. Green, P. Gallegos, M. Streeter, *et al.*, Proton acceleration using 50 fs, high intensity Astra-Gemini laser pulses, Nucl. Instrum. Methods Phys. Res. Sect. A: Accelerators, Spectrometers, Detectors and Associated Equip. **653**, 113 (2011).

[76] M. Allen, P. K. Patel, A. Mackinnon, D. Price, S. Wilks, and E. Morse, Direct Experimental Evidence of Back-Surface Ion Acceleration from Laser-Irradiated Gold Foils, Phys. Rev. Lett. **93**, 265004 (2004).

[77] A. Soloviev, K. Burdonov, S. Chen, A. Eremeev, A. Korzhimanov, G. Pokrovskiy, T. Pikuz, G. Revet, A. Sladkov, V. Ginzburg, *et al.*, Experimental evidence for short-pulse laser heating of solid-density target to high bulk temperatures, Sci. Rep. **7**, 1 (2017).

[78] D. Hey, M. Key, A. Mackinnon, A. MacPhee, P. Patel, R. Freeman, L. Van Woerkom, and C. Castaneda, Use of gafchromic film to diagnose laser generated proton beams, Rev. Sci. Instrum. **79**, 053501 (2008).

[79] M. Foord, P. Patel, A. Mackinnon, S. Hatchett, M. Key, B. Lasinski, R. Town, M. Tabak, and S. Wilks, MeV proton generation and efficiency from an intense laser irradiated foil, High Energy Density Phys. **3**, 365 (2007).

[80] J. Green, A. Robinson, N. Booth, D. Carroll, R. Dance, R. Gray, D. MacLellan, P. McKenna, C. Murphy, D. Rusby, *et al.*, High efficiency proton beam generation through target thickness control in femtosecond laser-plasma interactions, Appl. Phys. Lett. **104**, 214101 (2014).

[81] M. M. Allen, *Ion Acceleration from the Interaction of Ultra-Intense Lasers with Solid Foils* (University of California, Berkeley, 2004).

[82] F.-E. Brack, F. Kroll, L. Gaus, C. Bernert, E. Beyreuther, T. E. Cowan, L. Karsch, S. Kraft, L. A. Kunz-Schughart, E. Lessmann, *et al.*, Spectral and spatial shaping of laser-driven proton beams using a pulsed high-field magnet beamline, Sci. Rep. **10**, 1 (2020).

[83] N. Dover, M. Nishiuchi, H. Sakaki, M. Alkhimova, A. Y. Faenov, Y. Fukuda, H. Kiriyama, A. Kon, K. Kondo, K. Nishitani, *et al.*, Scintillator-based transverse proton beam profiler for laser-plasma ion sources, Rev. Sci. Instrum. **88**, 073304 (2017).

[84] C. Qin, H. Zhang, S. Li, N. Wang, A. Li, L. Fan, X. Lu, J. Li, R. Xu, C. Wang, *et al.*, High efficiency laser-driven proton sources using 3d-printed micro-structure, Commun. Phys. **5**, 1 (2022).

[85] T. Ceccotti, A. Lévy, H. Popescu, F. Réau, P. d'Oliveira, P. Monot, J. Geindre, E. Lefebvre, and P. Martin, Proton Acceleration with High-Intensity Ultrahigh-Contrast Laser Pulses, Phys. Rev. Lett. **99**, 185002 (2007).

[86] L. Cialfi, L. Fedeli, and M. Passoni, Electron heating in subpicosecond laser interaction with overdense and near-critical plasmas, Phys. Rev. E **94**, 053201 (2016).

[87] M. Yan, G. Hu, B. Liu, Z. Liu, R. Wu, and S. Wang, Optimization design of a fast neutron imaging collimator by genetic algorithm, J. Instrum. **15**, P12002 (2020).

[88] number Y. Lu, Z. Xu, L. Zhang, Z. Wang, T. Li, and M. S. Khan, Geant4 simulations of the neutron beam characteristics for ^{9}Be/^{7}Li targets bombarded by the low energy protons, Nucl. Instrum. Methods Phys. Res. Sect. B: Beam Interactions with Mater. Atoms **506**, 8 (2021).

[89] F. Poignant, S. Penfold, J. Asp, P. Takhar, and P. Jackson, Geant4 simulation of cyclotron radioisotope production in a solid target, Phys. Med. **32**, 728 (2016).

[90] F. James, A review of pseudorandom number generators, Comput. Phys. Commun. **60**, 329 (1990).